



State-Specific Modeling of Vibrational Relaxation and Nitric Oxide Formation in Shock-Heated Air

W. Su* and D. Bruno†

Consiglio Nazionale delle Ricerche, 70125 Bari, Italy

and

Y. Babou‡

Universidad Carlos III de Madrid, 28911 Madrid, Spain

DOI: 10.2514/1.T5271

A vibration-specific approach is employed to describe vibrational relaxation and reactive processes in shock-heated air. Models are implemented that include results from recent theoretical calculations for the relevant rate coefficients. Two sets of rate coefficients for the Zeldovich reactions of nitric oxide formation, derived from quasi-classical trajectory calculations, are compared. The relaxation kinetics, nitric oxide formation, and vibrational nonequilibrium behind the shock are discussed in detail. Results show that the nitric oxide formation kinetics is sensitive to the details of the adopted rate coefficients. The effect of the adopted kinetic descriptions (multitemperature, state-to-state) on the postshock plasma radiative signature is investigated. The predicted radiative contribution from the oxygen Schumann–Runge band is dominant in the spectral range 200–300 nm for shock speeds of 5–8 km/s. Comparison to shock-tube absolute intensity measurements has provided indications for improvement of nonequilibrium flow modeling. It is suggested that a kinetic treatment of the radiating electronic states may improve the agreement.

Nomenclature

A_{ul}	= Einstein coefficient for spontaneous emission, s^{-1}
c	= speed of light, cm/s
D	= shock-tube inner diameter, m
e	= specific energy, J/kg
f	= line profile, cm^{-1}
g	= level degeneracy
\mathbb{H}	= neutral species set: { N_2 , O_2 , NO, N, O}
h	= specific enthalpy, J/kg
h^{of}	= formation enthalpy, J/kg
h_P	= Planck's constant, Js
\mathbb{I}	= positive ion species set { N_2^+ , O_2^+ , NO ⁺ , N ⁺ , O ⁺ }
J	= rotational level
k_B	= Boltzmann's constant, J/K
k_{eq}	= reaction equilibrium constant, adimensional
N_A	= Avogadro's constant, mol^{-1}
n	= number density, $1/\text{m}^3$ or principal quantum number
p	= pressure, Pa
Q	= partition function
r	= specific gas constant, $\text{J}/(\text{kg} \cdot \text{K})$
s^p	= stoichiometric coefficient for products
s^r	= stoichiometric coefficient for reactants
T	= temperature, K
u	= hydrodynamic velocity, m/s
VT	= vibrational-translational energy exchange
v, w	= vibrational level
x	= abscissa along flow axis, m
y	= mass fraction
α, β, γ	= coefficients in Arrhenius function
ϵ	= vibrational level energy, J
η_σ	= spectral emission coefficient, $\text{W}/\text{m}^3/(\text{sr} \cdot \text{cm}^{-1})$

Received 29 May 2017; revision received 7 August 2017; accepted for publication 2 October 2017; published online 31 October 2017. Copyright © 2017 by the American Institute of Aeronautics and Astronautics, Inc. All rights reserved. All requests for copying and permission to reprint should be submitted to CCC at www.copyright.com; employ the ISSN 0887-8722 (print) or 1533-6808 (online) to initiate your request. See also AIAA Rights and Permissions www.aiaa.org/randp.

*Postdoctoral Fellow, Istituto di Nanotecnologia.

†Researcher, Istituto di Nanotecnologia.

‡Postdoctoral Fellow, Departamento de Bioingeniería Ingeniería Aeroespacial.

v^{max}	= maximum vibrational quantum number, zero for atoms
ρ	= mass density, kg/m^3
σ	= radiation wave number, cm^{-1}
τ	= relaxation time, s
Ω	= energy source term, $\text{J}/(\text{m}^3 \cdot \text{s})$
$\dot{\omega}$	= mass production rate, $\text{kg}/(\text{m}^3 \cdot \text{s})$

Subscripts

b	= backward
e	= free electron component
f	= forward
k	= species index; reaction rate constant, m^3/s
u, l	= upper, lower level

Superscripts

el	= electronic
eq	= equilibrium
rot	= rotational
tra	= translational
vib	= vibrational

I. Introduction

HIGH-SPEED entry of a spacecraft into a planetary atmosphere is one of the most critical mission phases. Improving available models' predictive capabilities allows one to reduce the design margins and has, therefore, a large impact on the overall mission mass and cost budgets. Large uncertainties remain in the prediction of the nonequilibrium zone behind the shock wave and in the emitted radiation field. This is true for shock conditions relevant to lunar and Mars return missions, where the reentry velocity exceeds 10 km/s and a large contribution to the radiative heat flux comes from atomic species. In these conditions, results are not sensitive to the details of the dissociation model nor to the vibration–chemistry coupling [1]; instead, electronic excitation by heavy particle impact, a nonadiabatic process, is shown to play a strong role.

At smaller shock speeds, relevant to entry from orbit and hypersonic commercial flights, most of the emitted radiation comes from molecular transitions, and so the radiation from the shocked gas is a valuable probe of the underlying relaxation kinetics. Particularly sensitive to the details of the relaxation kinetics is the concentration of

NO. Being a strong radiator, accurate prediction of the NO formation kinetics is crucial to the correct understanding of the flow radiation signature.

Nowadays, vibrational state-specific rate coefficients from ab initio calculations are becoming available to describe vibrational relaxation and reactive processes in air. Advanced models, which include results from theoretical calculations of state-specific rate coefficients, have been applied to study shock waves in nitrogen [2–6] or oxygen [7,8]. Few works have considered the vibrational–chemical kinetics of shock-heated air [9–11]. In these works, the vibrational-specific description was limited to N₂ and O₂ only. Recently, Lopez and da Silva [12] applied a vibrationally specific model to the investigation of NO formation in hypersonic flows in air.

In this study, we simulate the nonequilibrium relaxation in shock-heated air with a vibrationally specific approach. The NO formation kinetics is discussed in detail and a comparison is made on the results obtained by two sets of rate coefficients for the Zeldovich reactions of NO formation [13–17]. Worth mentioning, in this respect, are two recent works investigating the kinetics of O₂ + N [18] and N₂ + O [19] processes, which are based on quasi-classical trajectory (QCT) studies on the same potential energy surfaces (PESs) as those by Esposito and Armenise [15], Armenise and Esposito [16], and Capitelli et al. [17]. Then, to assess the reliability of the investigated kinetic models, the flow radiative signature is determined on the basis of the spectroscopic database HTGR [20] and compared with shock-tube experimental results [21].

The remainder of the paper is organized as follows. In Sec. II, the numerical modeling is described, including the methods used to obtain the state-specific rate constants; in Sec. III, the modeling is applied to simulate postshock relaxation flows. The flow properties, kinetics of translational-vibrational-chemical coupling, and vibrational distributions are discussed. Section IV discusses the flow radiative properties and compares the results to the shock-tube measurements made in the double diaphragm shock tube at Moscow State University [21]. Conclusions are summarized in Sec. V.

II. Modeling

For the shock conditions of interest ($v \sim 5\text{--}8 \text{ km/s}$), the ionization degree is expected to be small. As a first step, we therefore consider a gas mixture composed of the five chemical species N₂, O₂, NO, N, and O in their ground electronic state. This allows us to emphasize the coupling of translational, vibrational, and chemical kinetics. To compute the radiative properties, the model will then be extended to include ionization and this assumption justified.

A. Governing Equations for Nonionized Air

The translational and rotational modes are assumed to thermalize quickly and follow Maxwell–Boltzmann distributions at the gas temperature T . A state-specific description is adopted instead for the vibrational modes of diatomic molecules that allows us to study the thermal nonequilibrium zone. Oscillator levels are taken from [12], which gives 61 bound levels for N₂, 46 levels for O₂, and 48 for NO. In the frame of reference moving with the shock, the flow is then conveniently described by the stationary, inviscid one-dimensional Euler equations:

$$\begin{aligned}\partial_x(\rho u) &= 0 \\ \partial_x(\rho u y_k^v) &= \dot{\omega}_k^v, \quad v = 0, \dots, v_{\max}^k, \quad k \in \mathbb{H} \\ \partial_x(\rho u^2 + p) &= 0 \\ \partial_x \left[\rho u \left(h + \frac{u^2}{2} \right) \right] &= 0\end{aligned}\quad (1)$$

Species mass fractions are obtained by summing over vibrational levels:

$$y_k = \sum_{v=0}^{v_{\max}^k} y_k^v \quad (2)$$

These governing equations are completed by the equations of state that relate p , T , h and by the chemical network of processes and related rate coefficients that define the source terms $\dot{\omega}_k^v$. The equations of state are those of the ideal gas with separable degrees of freedom:

$$p = \rho \sum_{k \in \mathbb{H}} y_k r_k T \quad (3)$$

$$h = \sum_{k \in \mathbb{H}} y_k (e_k^{\text{tra}} + r_k T + e_k^{\text{rot}} + e_k^{\text{vib}} + h_k^{\text{0f}}) \quad (4)$$

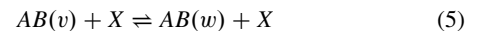
where

$$e_k^{\text{vib}} = \sum_{v=0}^{v_{\max}^k} \frac{y_k^v}{y_k} e_k^v$$

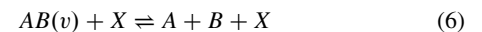
The chemical network is discussed in detail in the next sections. Equations (1–4) are solved by the ODEPACK library [22].

B. Vibrational–Chemical Kinetic Mechanism in Nonionized Air

Three types of processes are included: 1) vibrational-translational (VT) energy exchange



2) dissociation-recombination (DR) reactions



and 3) Zeldovich exchange (ZE) reactions [23]



Values for the state-specific rate coefficients are obtained, where available, from QCT calculations and the semi-analytical forced harmonic oscillator (FHO) model. For the remaining processes, where none of the preceding is available, the classical models of Landau–Teller (LT) relaxation and Park’s two-temperature models are used. Table 1 summarizes the state-specific reactions considered in this work and the methods used to calculate the reaction rate constants.

1. State-Specific Rates from FHO and QCT Calculations

The state-specific rates for vibrational excitation and dissociation in diatom–diatom collisions are taken from the STELLAR database[§]; it collects results from the work of da Silva et al. [24], who applied the FHO model [25] to the production of data sets of multiquantum VT and DR rates in a wide temperature range. The excitation and dissociation rates for N₂–N and O₂–O systems are from the work of Esposito et al. [26,27], which produced complete sets of vibrational specific rates from QCT calculations. For the two Zeldovich exchange reactions, two alternative data sets are available, both obtained from QCT calculations: one based on the classical work of Bose and Candler [13,14] (Bose’s rates in the following) and the other from the very recent work by Esposito and Armenise [15], Armenise and Esposito [16], and Capitelli et al. [17] (Esposito’s rates).

In the latter case, the new PESs developed by Sayos et al. [28] and Gamallo et al. [29] have been used. The dissociation rates in N₂–O and O₂–N collisions are also from these works. The accuracy of the new rates has been demonstrated by comparison with measured thermal rate coefficients [15] and with quantum calculations [30]. All vibrationally specific rates (both from FHO and QCT) are obtained from cross sections rotationally averaged at $T_{\text{rot}} = T$.

[§]Data available online at <http://esther.ist.utl.pt/pages/stellar.html> [retrieved 10 January 2016].

Table 1 Vibrational–chemical kinetic mechanism

Reaction	Model	Reaction	Model
$\text{N}_2(v) + \text{N}_2 \rightleftharpoons \text{N}_2(w) + \text{N}_2$	FHO	$\text{N}_2(v) + \text{N} \rightleftharpoons 3\text{N}$	QCT
$\text{N}_2(v) + \text{O}_2 \rightleftharpoons \text{N}_2(w) + \text{O}_2$	FHO	$\text{N}_2(v) + \text{O} \rightleftharpoons 2\text{N} + \text{O}$	QCT
$\text{N}_2(v) + \text{N} \rightleftharpoons \text{N}_2(w) + \text{N}$	QCT	$\text{N}_2(v) + \text{NO} \rightleftharpoons 2\text{N} + \text{NO}$	Park
$\text{N}_2(v) + X_1 \rightleftharpoons \text{N}_2(w) + X_1^a$	LT	$\text{O}_2(v) + \text{N}_2 \rightleftharpoons 2\text{O} + \text{N}_2$	FHO
$\text{O}_2(v) + \text{N}_2 \rightleftharpoons \text{O}_2(w) + \text{N}_2$	FHO	$\text{O}_2(v) + \text{O}_2 \rightleftharpoons 2\text{O} + \text{O}_2$	FHO
$\text{O}_2(v) + \text{O}_2 \rightleftharpoons \text{O}_2(w) + \text{O}_2$	FHO	$\text{O}_2(v) + \text{O} \rightleftharpoons 3\text{O}$	QCT
$\text{O}_2(v) + \text{O} \rightleftharpoons \text{O}_2(w) + \text{O}$	QCT	$\text{O}_2(v) + \text{N} \rightleftharpoons 2\text{O} + \text{N}$	QCT
$\text{O}_2(v) + X_2 \rightleftharpoons \text{O}_2(w) + X_2^b$	LT	$\text{O}_2(v) + \text{NO} \rightleftharpoons 2\text{O} + \text{NO}$	Park
$\text{NO}(v) + \text{N}_2 \rightleftharpoons \text{NO}(w) + \text{N}_2$	FHO	$\text{NO}(v) + \text{N}_2 \rightleftharpoons \text{N} + \text{O} + \text{N}_2$	FHO
$\text{NO}(v) + \text{O}_2 \rightleftharpoons \text{NO}(w) + \text{O}_2$	FHO	$\text{NO}(v) + \text{O}_2 \rightleftharpoons \text{N} + \text{O} + \text{O}_2$	FHO
$\text{NO}(v) + X_3 \rightleftharpoons \text{NO}(w) + X_3^c$	LT	$\text{NO}(v) + X_3 \rightleftharpoons \text{N} + \text{O} + X_3^c$	Park
$\text{N}_2(v) + \text{N}_2 \rightleftharpoons 2\text{N} + \text{N}_2$	FHO	$\text{N}_2(v) + \text{O} \rightleftharpoons \text{NO}(w) + \text{N}$	QCT
$\text{N}_2(v) + \text{O}_2 \rightleftharpoons 2\text{N} + \text{O}_2$	FHO	$\text{O}_2(v) + \text{N} \rightleftharpoons \text{NO}(w) + \text{O}$	QCT

^a $X_1 \in \{\text{NO}, \text{O}\}$.^b $X_2 \in \{\text{NO}, \text{N}\}$.^c $X_3 \in \{\text{NO}, \text{N}, \text{O}\}$.

2. State-Specific Rates from Classical Models

For some processes, state-specific rate coefficients are not available; we therefore resort to the classical models of LT relaxation (for VT) and Park's two-temperature model (for DR). This, however, does not specify the state-specific rate coefficients unambiguously. The approach adopted here is therefore detailed next. According to the LT model, the energy source term due to VT energy transfer in $AB - X$ collisions reads:

$$\Omega_{\text{VT}} = \rho_{AB} \frac{e_{AB}^{\text{vib},\text{eq}}(T) - e_{AB}^{\text{vib}}}{\tau_{AB-X}} \quad (8)$$

The relaxation time τ_{AB-X} is obtained from Millikan–White's formula [31]. In a state-to-state (StS) framework, this global behavior is recovered by choosing the state-specific rates for reactions $AB(v) + X \rightleftharpoons AB(w) + X$ as

$$k_f^{v \rightarrow w} = \frac{1}{N_A[X]} \cdot \left(\frac{y_{AB}^w}{y_{AB}} \right)^{\text{eq}} \cdot \frac{1}{\tau_{AB-X}}, \quad k_b^{v \rightarrow w} = k_f^{w \rightarrow v} \quad (9)$$

where $(y_{AB}^w/y_{AB})^{\text{eq}}$ is the reduced vibrational population at thermal equilibrium. Backward rates are calculated from the detailed balance condition, with

$$k_{\text{eq}}^{v \rightarrow w} = \exp \left(-\frac{e_{AB}^w - e_{AB}^v}{k_B T} \right)$$

As for DR processes, according to Park's model ([32] pp. 112–115), the rate coefficients are expressed as modified Arrhenius functions:

$$\begin{aligned} k_f(T_f) &= \alpha_f \cdot T_f^{\beta_f} \cdot \exp \left(-\frac{\gamma_f}{T_f} \right) \\ k_{\text{eq}}(T_b) &= \alpha_b \cdot T_b^{\beta_b} \cdot \exp \left(-\frac{\gamma_b}{T_b} \right) \\ k_b(T_b) &= \frac{k_f(T_b)}{k_{\text{eq}}(T_b)} \end{aligned} \quad (10)$$

where $T_f = \sqrt{T \cdot T_{\text{vib}}}$, $T_b = T$. The preceding behavior is reproduced by choosing

$$\begin{aligned} k_f^v &= k_f \cdot \prod_{k \in H} \left(\frac{\exp(-e_k^v/k_B T_k^{\text{vib}})}{\sum_w \exp(-e_k^w/k_B T_k^{\text{vib}})} \right)^{s_k^p} \\ k_b^v &= k_b \cdot \prod_{k \in H} \left(\frac{\exp(-e_k^v/k_B T_k^{\text{vib}})}{\sum_w \exp(-e_k^w/k_B T_k^{\text{vib}})} \right)^{s_k^r} \end{aligned} \quad (11)$$

This choice also defines the chemistry–vibration coupling. The average vibrational energy lost/gained in reaction is given by

$$\langle e_{k,f} \rangle = \langle e_{k,b} \rangle = e_{\text{vib}}^k(T_{\text{vib}}) \quad (12)$$

so that the reaction has a nonpreferential character, in agreement with the spirit of the original model. Values for the model parameters in Eq. (10) are taken from [21].

C. Modeling of Ionized Air

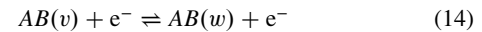
To give a reasonable estimation for the postshock radiative signature, a model able to describe the ionization kinetics is required. Only singly ionized positive ions are considered, and so now the gas mixture includes 11 species: N_2 , O_2 , NO , N , O , N_2^+ , O_2^+ , NO^+ , N^+ , O^+ , e^- . In the absence of external electromagnetic fields, it is expected that no charge separation nor currents appear, and charged species are considered to be in the ambipolar diffusion regime ([32] pp. 129–133). Equations (1) can then be readily extended to the present case, with the addition of a conservation equation for the energy of free electrons:

$$\partial_x[\rho u e_e(T_e)] + p_e \partial_x u = \Omega_e \quad (13)$$

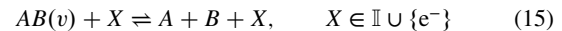
In this equation, the specific energy $e_e(T_e)$ includes contributions from all energy reservoirs in equilibrium at the free electron temperature T_e , which is the case of the vibrational modes of the molecular ions.

Besides the kinetic mechanism in Table 1, five additional types of processes are included as follows:

- 1) Electron impact vibrational excitation (e-V)



- 2) Ions or electron impact dissociation–recombination reactions



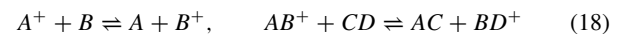
- 3) Associative ionization (AI)



- 4) Electron-impact ionization (EI)



- 5) Charge exchange (CE) reactions



The detailed additional reactions considered for ionized flows are summarized in Table 2. The state-specific reaction rates for

Table 2 Additional vibrational–chemical kinetic mechanism for ionized air

Reaction	Model	Reaction	Model
$\text{N}_2(v) + \text{e}^- \rightleftharpoons \text{N}_2(w) + \text{e}^-$	LCP	$\text{O}_2^+ + \text{N}_2(v) \rightleftharpoons \text{O}_2(w) + \text{N}_2^+$	Park
$\text{O}_2(v) + \text{e}^- \rightleftharpoons \text{O}_2(w) + \text{e}^-$	LCP	$\text{NO}^+ + \text{N}_2(v) \rightleftharpoons \text{NO}(w) + \text{N}_2^+$	Park
$\text{NO}(v) + \text{e}^- \rightleftharpoons \text{NO}(w) + \text{e}^-$	LCP	$\text{O}_2^+ + \text{N} \rightleftharpoons \text{O}_2(v) + \text{N}^+$	Park
$\text{N}_2(v) + \text{e}^- \rightleftharpoons 2\text{N} + \text{e}^-$	LCP	$\text{O}_2^+ + \text{O} \rightleftharpoons \text{O}_2(v) + \text{O}^+$	Park
$\text{O}_2(v) + \text{e}^- \rightleftharpoons 2\text{O} + \text{e}^-$	LCP	$\text{O}^+ + \text{N}_2(v) \rightleftharpoons \text{O} + \text{N}_2^+$	Park
$\text{N}_2(v) + X_1 \rightleftharpoons 2\text{N} + X_1^a$	Park	$\text{NO}^+ + \text{O} = \text{NO}(v) + \text{O}^+$	Park
$\text{O}_2(v) + X_1 \rightleftharpoons 2\text{O} + X_1^a$	Park	$\text{NO}^+ + \text{O}_2(v) \rightleftharpoons \text{NO}(v) + \text{O}_2^+$	Park
$\text{NO}(v) + X_2 \rightleftharpoons \text{N} + \text{O} + X_2^b$	Park	$\text{N}_2(v) + \text{N}^+ \rightleftharpoons \text{N}_2^+ + \text{N}$	Park
$X_3 + \text{e}^- \rightleftharpoons X_3^+ + 2\text{e}^-c$	Park	$\text{NO}^+ + \text{NO}(v) \rightleftharpoons \text{N}_2(w) + \text{O}_2^+$	Park
$\text{N} + \text{N} \rightleftharpoons \text{N}_2^+ + \text{e}^-$	Park	$\text{NO}^+ + \text{NO}(v) \rightleftharpoons \text{O}_2(w) + \text{N}_2^+$	Park
$\text{O} + \text{O} \rightleftharpoons \text{O}_2^+ + \text{e}^-$	Park	$\text{NO}^+ + \text{N} \rightleftharpoons \text{N}_2(v) + \text{O}^+$	Park
$\text{N} + \text{O} \rightleftharpoons \text{NO}^+ + \text{e}^-$	Park	$\text{NO}^+ + \text{N} \rightleftharpoons \text{N}_2^+ + \text{O}$	Park
$\text{O} + \text{N}^+ \rightleftharpoons \text{O}^+ + \text{N}$	Park	$\text{NO}^+ + \text{O} \rightleftharpoons \text{O}_2(v) + \text{N}^+$	Park
$\text{N}_2^+ + \text{O} \rightleftharpoons \text{NO}(v) + \text{N}^+$	Park	$\text{NO}^+ + \text{O} = \text{O}_2^+ + \text{N}$	Park

^a $X_1 \in \mathbb{I}$.^b $X_2 \in \mathbb{I} \cup \{\text{e}^-\}$.^c $X_3 \in \mathbb{H}$.

electron-impact resonant vibrational excitation and dissociation are from the work of Laporta et al. [33–36]. The cross sections were computed using local complex potential (LCP) models and the reaction rate constants derived assuming an equilibrium distribution for the electron energy. The effect of the rotational state, assumed conserved in the transition, was also estimated by computing the cross sections at rotational state $J = 0, 50, 100$, and 150 . The behavior, as well as the order of magnitude of the cross sections with $J = 50, 100$, and 150 , is comparable to those with $J = 0$. Thereby, only the data with $J = 0$ have been used.[¶]

For other reactions, the state-specific rates are again derived from Park's model ([32] pp. 112–115). In these cases, the controlling temperatures in forward and backward reactions are given by

Electron impact DR:

$$T_f = \sqrt{T_e \cdot T_{\text{vib}}}, \quad T_b = T_e \quad (19)$$

AI and EI:

$$T_f = T_e, \quad T_b = T_e \quad (20)$$

CE:

$$T_f = T, \quad T_b = T \quad (21)$$

In the conservation equation (13), the source term for the electron energy Ω_e includes contributions from [5,37] elastic collisions between electrons and heavy particles; relaxation of the rotational modes of diatoms due to electron impact; the relaxation of the vibrational modes of N_2 , O_2 , and NO in e-V collisions; and the energy exchanged in chemical reactions involving N_2^+ , O_2^+ , NO^+ , e^- .

III. Results and Discussion

We consider shock waves propagating at $u_1 = 5.0$ – 8.06 km/s in mixtures of N_2 and O_2 (80–20% molar fraction composition) at $T_1 = 298$ K, $p_1 = 0.25$ /1.0 torr. The shock speed and upstream pressure for each case are summarized in Table 3. The downstream conditions just behind the shock are obtained from the Rankine–Hugoniot jump relations assuming frozen chemistry and vibrational kinetics. The detailed state-to-state approach is used to solve for the evolution of the flow behind the shock waves. We employed two different models of state-specific rates for the Zeldovich exchange reactions (i.e., Esposito's and Bose's rates, labeled as ‘‘Esopo’’ and

Table 3 Upstream pressure and shock speed for the shock waves considered

Case index	u_1 , km/s	p_1 , torr
1	5.00	1.0
2	5.38	1.0
3	5.56	1.0
4	5.90	1.0
5	6.10	1.0
6	6.41	1.0
7	6.49	1.0
8	6.76	1.0
9	6.94	1.0
10	7.14	0.25
11	8.06	0.25

‘‘Bose’’ in the plots). Results obtained by a standard multitemperature (MT) approach [21] are also shown for comparison.

Two representative cases at low (Sec. III.A) and high (Sec. III.B) shock speeds are discussed, and differences in the results produced with the two data sets are analyzed; Sec. III.C illustrates vibrational distributions along the flow, and Sec. III.D summarizes the results on NO formation.

A. Relaxation in Five-Species Air at Low Shock Speeds

As a representative low-speed case, we discuss results for the shock with $u_1 = 5.56$ km/s, $p_1 = 1.0$ torr. Figure 1 shows temperatures and composition profiles. Differences between Esopo and Bose models are only noticeable for the vibrational temperature and abundance of NO. Esposito's rates predict a slightly larger formation than Bose's rates. This is because Bose's rates produce NO at much larger vibrational temperature.

The differences, however, are restricted to a sub-millimeter region behind the shock and are unlikely to be measured experimentally. The MT model, instead, predicts sensibly slower relaxation and lower NO production. This also affects the concentration of molecular oxygen at larger length scales.

B. Relaxation in Five-Species Air at High Shock Speeds

Figure 2 shows temperature profiles (Fig. 2a) and species mole fractions (Fig. 2b) for the shock with $u_1 = 8.06$ km/s, $p_1 = 0.25$ torr. The two models for the ZE reactions result in large differences in the predicted evolution of the NO vibrational temperature. Esposito's rates create NO at about 16,000 K, which then increases to its maximum value at about 18,000 K due to excitation; Bose's rates, instead, create NO at 32,500 K, then it increases to about 40,000 K, which is higher than the gas temperature. Again, Esposito's

[¶]Data available online at <http://phys4entrydb.ba.imip.cnr.it/Phys4EntryDB/> [retrieved 25 May 2016].

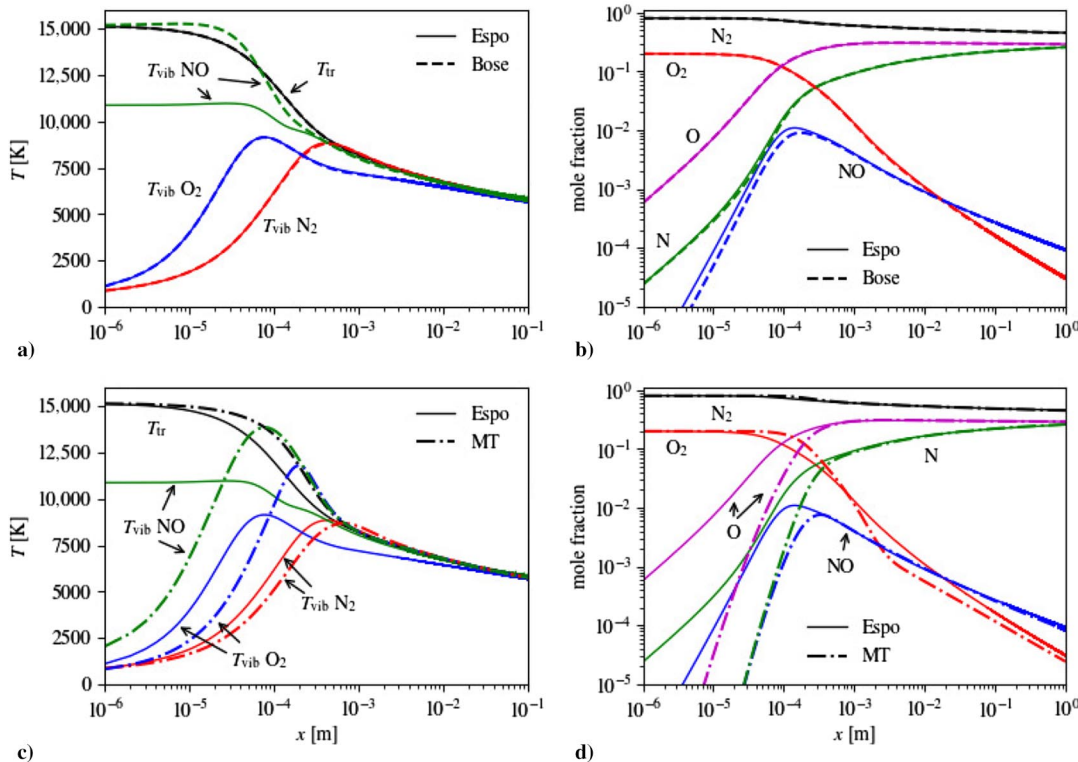


Fig. 1 Relaxation behind the shock ($u_1 = 5.56$ km/s, $p_1 = 1.0$ torr). Comparison of results obtained with different kinetic models: a,c) temperature profiles; b,d) composition profiles.

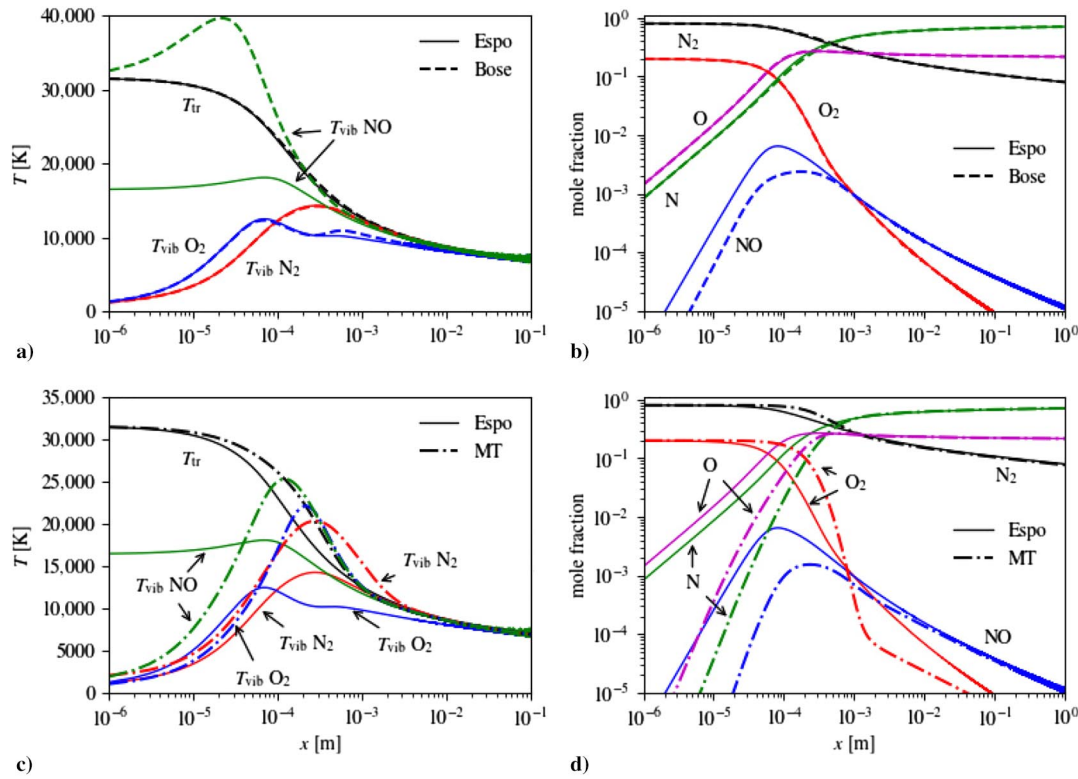


Fig. 2 Relaxation behind the shock ($u_1 = 8.06$ km/s, $p_1 = 0.25$ torr). Comparison of results obtained with different kinetic models: a,c) temperature profiles; b,d) composition profiles.

rates predict larger NO formation than Bose's rates. Compared with the MT model, both state-specific models predict faster relaxation and a large vibrational temperature for the nascent NO population.

Analysis of the vibrational energy source terms helps in identifying the main mechanisms responsible for this behavior. These are defined as

$$\Omega_i = \sum_{v=0}^{v_{AB}^{\max}} \dot{\omega}_{AB,i}^v \epsilon_{AB}^v, \quad i \in \{VT, DR, ZE\} \quad (22)$$

The VT energy source term is positive when the vibrational temperature is lower than the gas temperature and energy flows into

the vibrational mode; the DR and ZE terms are positive when the species is produced. The VT source term for NO from Esposito's rates rises first, then drops to accommodate the change in the amount of substance, but it stays positive (shown later). On the other hand, Bose's rates predict that NO is created at temperatures higher than the translational one and the corresponding VT source term first quickly falls to the negative minimum value and then gradually increases to positive values due to deexcitation and dissociation processes. At about 1.9×10^{-4} m, dissociation outweighs the exchange processes, a strong depletion of the species makes the vibrational temperature drop below the translational temperature, and this source term becomes positive. After that, the coupling effects of excitation and dissociation make the VT source term increase first, then decrease to zero.

Because the gas temperature is larger in this case, multiquanta dissociation of N_2 is enhanced, and so the formation of NO starts by consuming O_2 (shown later). As the dissociation of O_2 proceeds, this reaction reverses its sign and the other exchange reaction becomes the major contribution to NO production (Fig. 3a). Differences between the two models are clearly a consequence of the different vibrational temperature at which NO is produced, which are reflected in the VT term (shown later).

We also define preferential energy source terms for DR and ZE processes as

$$\Omega_i^{\text{Pref}} = \Omega_i - \dot{\omega}_{AB,i} \cdot e_{AB}^{\text{vib}}, \quad i \in \{\text{VT}, \text{DR}\} \quad (23)$$

These terms express the preferentiality of the chemistry–vibration coupling and are directly related to the evolution of the vibrational temperatures produced by the chemical reaction.

It is well known that nitrogen dissociation has a clear preferential character and it draws vibrational energy as it proceeds, and this is confirmed by the simulations as shown in Fig. 3: the preferential energy source term is of the same order of magnitude of the energy source term. The same is true for O_2 (Fig. 4). This character is much less pronounced for the other dissociation reaction (Fig. 5): The preferential DR energy source term is about 30 times smaller than the nonpreferential one. Note that, although Bose's rates produce less NO than Esposito's, the former absorb more N_2 vibrational energy than the latter (Fig. 3b). However, these source terms are much smaller than either the VT and DR ones, and so their influence on the

N_2 vibrational temperature is small. The alternating behavior of the exchange reaction involving O_2 , instead, produces nonmonotonic behavior of the O_2 vibrational temperature, as seen in Fig. 2; this is particularly true for the Bose's model, which features a stronger preferential character (Fig. 4b).

C. Vibrational Distributions

The state-specific models provide information on the vibrational distribution functions (VDFs) of diatomic molecules along the flow and it is interesting to analyze their behavior. Calculations show that the behavior of VDFs is similar in all cases and that the degree of vibrational nonequilibrium increases with the shock speed, as expected. Plots are then shown for the $u_1 = 8.06 \text{ km/s}$, $p_1 = 0.25 \text{ torr}$ case only.

Figure 6 shows the locations along the flow at which VDFs for N_2 are plotted. The calculated VDFs, together with the Boltzmann distribution functions at the equivalent vibrational temperatures, are illustrated in Fig. 7. Close to the shock (Fig. 7a), the VDF features a large overpopulation of the high-lying vibrational levels due to multiquanta VT processes. Then, as excitation and dissociation proceeds, the VDF gradually tends toward a Boltzmann distribution (Fig. 7b). However, as dissociation proceeds, the distribution shows the characteristic depletion of high-lying levels, typical of vibrationally favored reactions.

Figures 8 and 9 show the locations and VDFs for O_2 ; the behavior is similar to that of N_2 . It is interesting to note that differences in the high-lying level populations predicted by Esposito's and Bose's rates are observed at $x_{\max \text{O}_2}$ and $x_{0.001}$. Esposito's rates predict larger underpopulation of the high-lying vibrational levels. The discrepancy appears after the exchange reaction $\text{O}_2(v) + \text{N} \rightleftharpoons \text{NO}(w) + \text{O}$ starts proceeding predominantly in the backward direction.

Figures 10 and 11 show the locations and VDFs for NO. It shows that both Esposito's and Bose's results are close to the Boltzmann distribution functions at all three locations. However, VDFs predicted by Bose's rates do not show significant underpopulation of the high-lying vibrational levels.

D. Summary

In this section, the main results concerning NO formation are summarized. The maximum NO mole fraction and its position behind

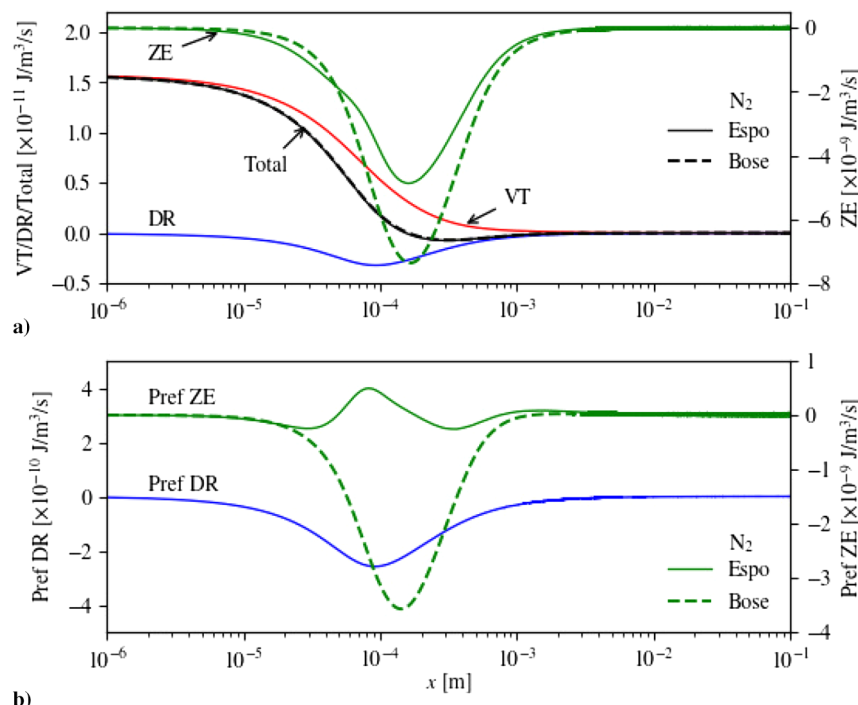


Fig. 3 Vibrational energy source terms of N_2 ($u_1 = 8.06 \text{ km/s}$, $p_1 = 0.25 \text{ torr}$): a) VT, DR, ZE, and total energy source terms; b) preferential DR and ZE energy source terms.

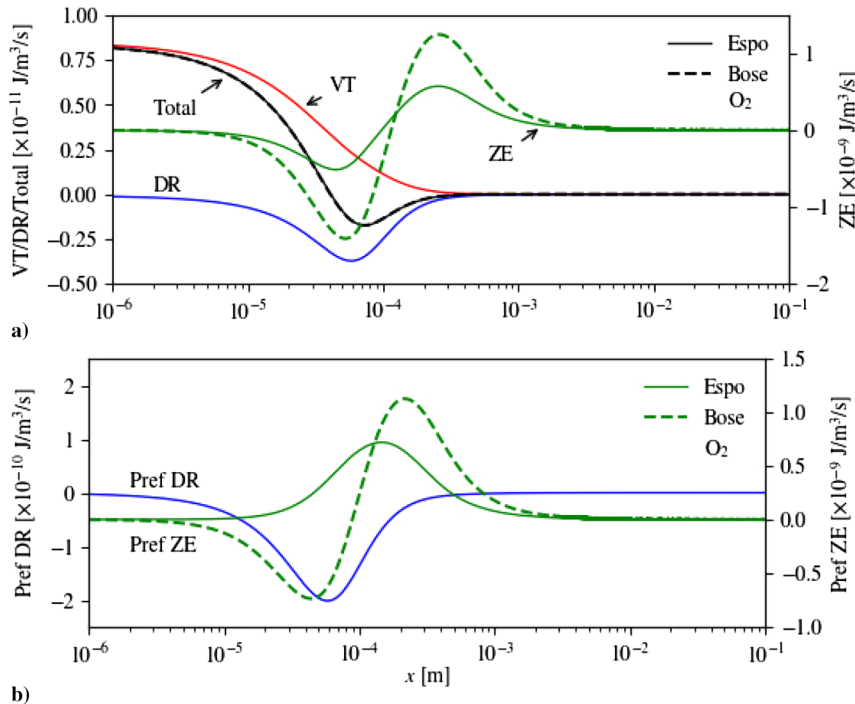


Fig. 4 Vibrational energy source terms of O_2 ($u_1 = 8.06 \text{ km/s}$, $p_1 = 0.25 \text{ torr}$): a) VT, DR, ZE, and total energy source terms; b) preferential DR and ZE energy source terms.

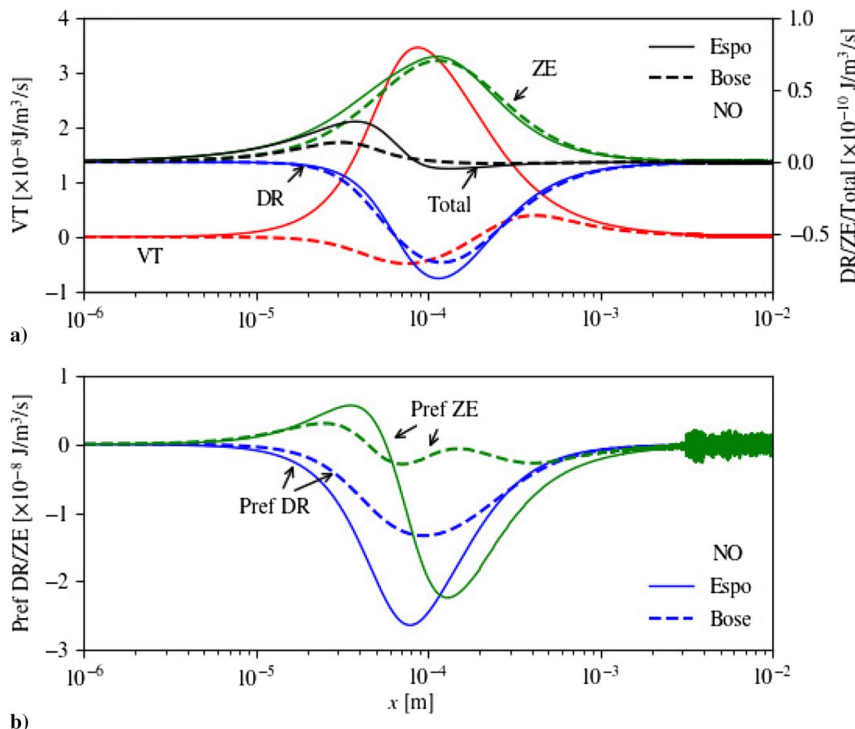


Fig. 5 Vibrational energy source terms of NO ($u_1 = 8.06 \text{ km/s}$, $p_1 = 0.25 \text{ torr}$): a) VT, DR, ZE, and total energy source terms; b) preferential DR and ZE energy source terms.

the shock are shown in Fig. 12 as a function of shock speed. The position has been normalized by λ_1 , the upstream mean free path, which is estimated from the coefficient of shear viscosity as 4.71×10^{-5} and 1.88×10^{-4} m for the 1 and 0.25 torr cases, respectively. The shift of the maximum to earlier times, predicted by all models, is clearly a result of the larger gas temperature that promotes faster dissociation (Fig. 12b). Also worth noting is that the state-specific models predict faster relaxation than the MT model, even though both feature a noticeable vibrational favoring of the dissociation reactions.

In spite of the depletion of the high vibrational levels, fast relaxation is supported by the increase of multiquanta processes that allow dissociation from low vibrational levels [5]. This result could be of interest also at larger shock speeds where MT models have been shown to produce too slow a relaxation, particularly when a preferential vibration–chemistry coupling is considered [1]. The formation of NO results from the competition between the Zeldovich exchange reactions and the dissociation reactions. Both reactions are enhanced by a larger gas temperature, so that relative differences in the temperature

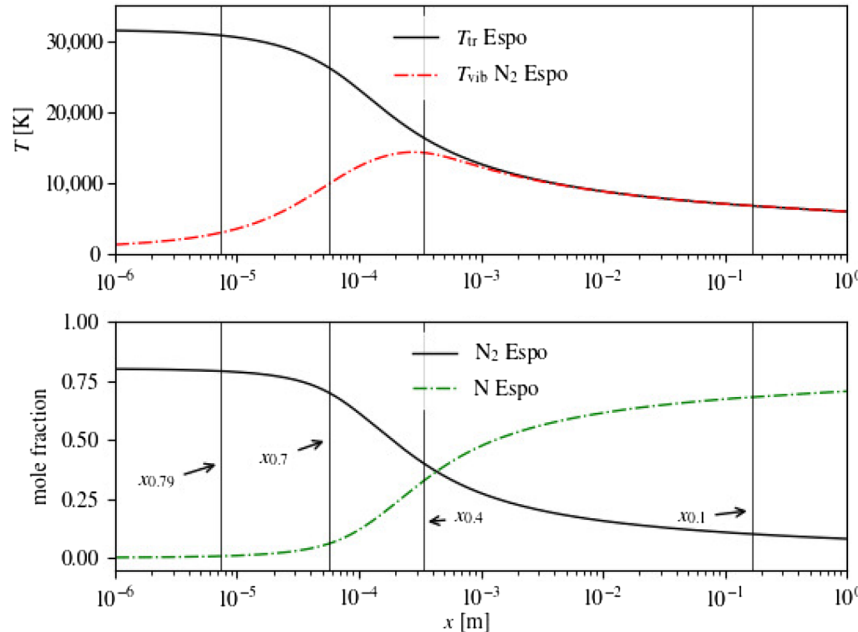


Fig. 6 Locations where vibrational distribution functions for N_2 are sampled ($u_1 = 8.06 \text{ km/s}$, $p_1 = 0.25 \text{ torr}$).

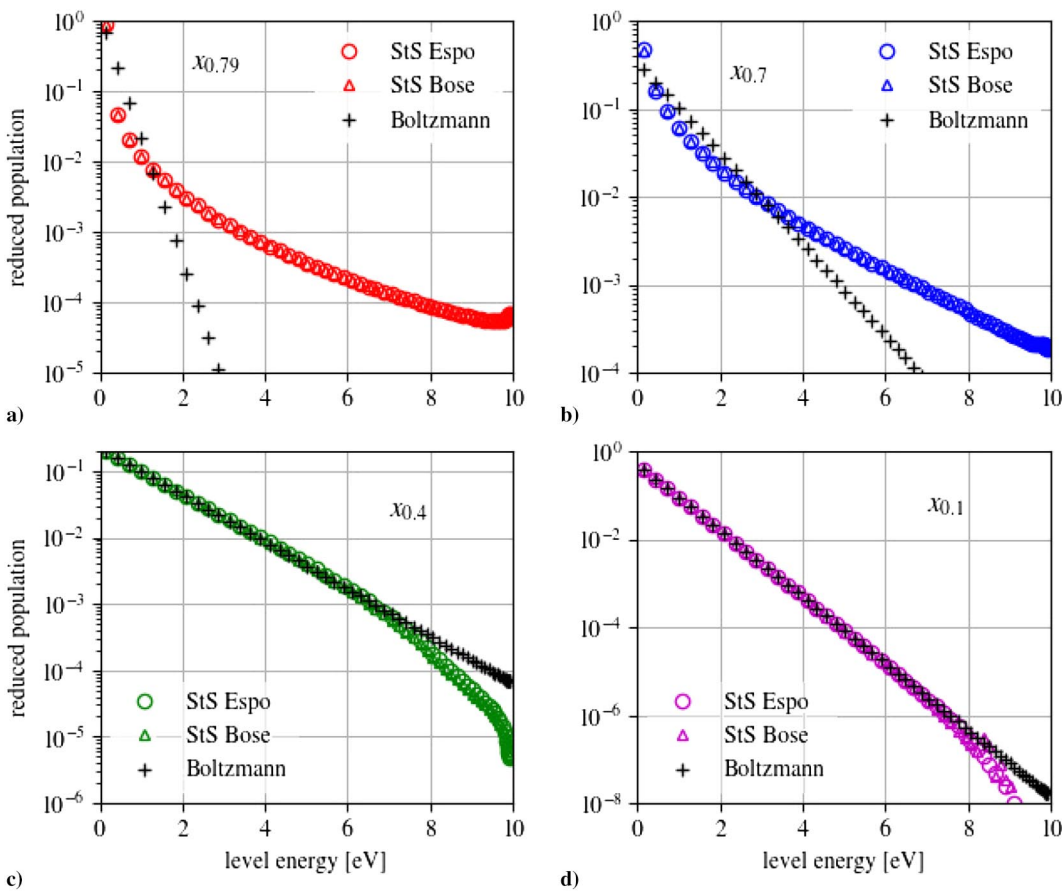


Fig. 7 Vibrational distribution functions of N_2 as obtained in the state-specific models. The Boltzmann distribution at the equivalent T_{vib} is also plotted for comparison: a) $x_{0.79}$; b) $x_{0.7}$; c) $x_{0.4}$; d) $x_{0.1}$.

dependence of these rates can explain the difference in the results produced by different models. Whereas the MT model predicts a monotonic decrease of the NO maximum with shock speed, both vibrationally specific models predict larger NO formation as a result of a more balanced competition of formation and dissociation processes. Results obtained with Esposito's rates show that NO formation goes through a broad maximum at $u_1 \approx 5.5 \text{ km/s}$.

Another important result, not obtained with the MT model, is the large vibrational temperature of the nascent NO population. A detailed investigation of the rate coefficients of both models shows that Bose's rates forming high-lying vibrational levels of NO are significantly larger than Esposito's. This explains the vibrational temperature overshoot predicted with the former model. On the other hand, Esposito's rates are larger for the

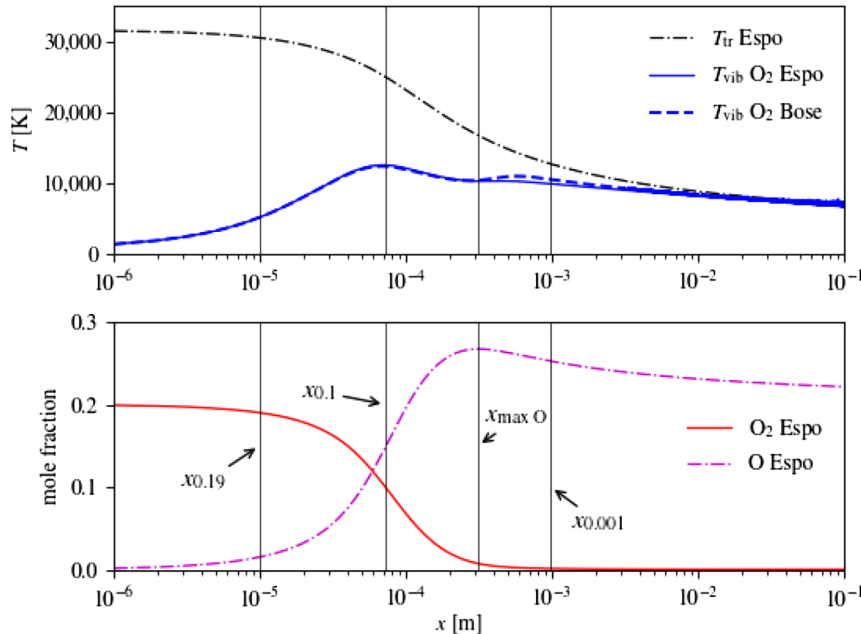


Fig. 8 Locations where vibrational distribution functions for O_2 are sampled ($u_1 = 8.06 \text{ km/s}$, $p_1 = 0.25 \text{ torr}$).

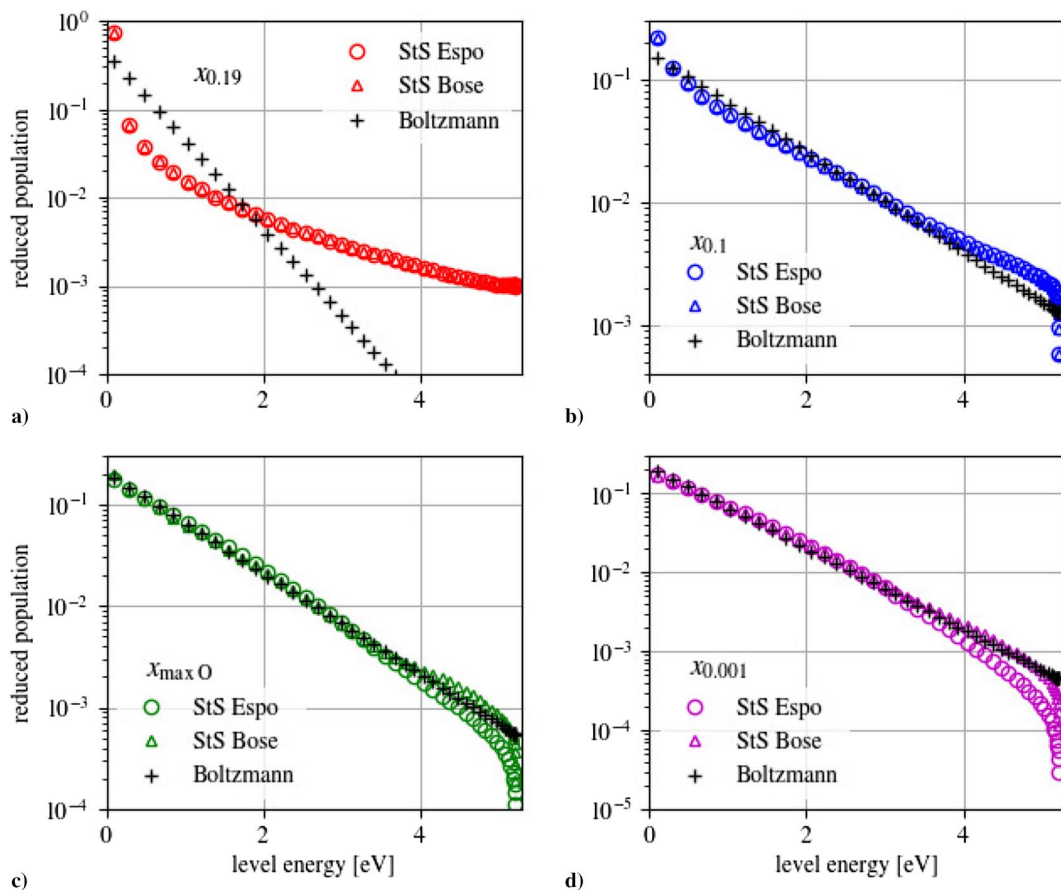


Fig. 9 Vibrational distribution functions of O_2 as obtained in the state-specific models. The Boltzmann distribution at the equivalent T_{vib} is also plotted for comparison: a) $x_{0.19}$; b) $x_{0.1}$; c) $x_{\max \text{O}}$; d) $x_{0.001}$.

formation of NO in intermediate-lying states. This leads to a larger production of NO. Note, however, that the original work [13,14] only reported calculated rates for low and intermediate vibrational levels. Data for high-lying vibrational levels are obtained by extrapolation [12].

To check that the preceding results are not appreciably modified when ionization is taken into account, the calculations have been repeated with an extended model for 11-species air, as detailed in

Sec. II.C. In all cases, the ionization degree is low and the results obtained with the extended model do not differ appreciably from those obtained with the five-species model. This is shown in Fig. 13 for the $u_1 = 8.06 \text{ km/s}$, $p_1 = 0.25 \text{ torr}$ case and the Espo model; but the same is true for all cases and all tested models. However, the 11-species model provides results for the electron temperature and the concentration of N_2^+ , which are essential inputs for the radiation calculation.

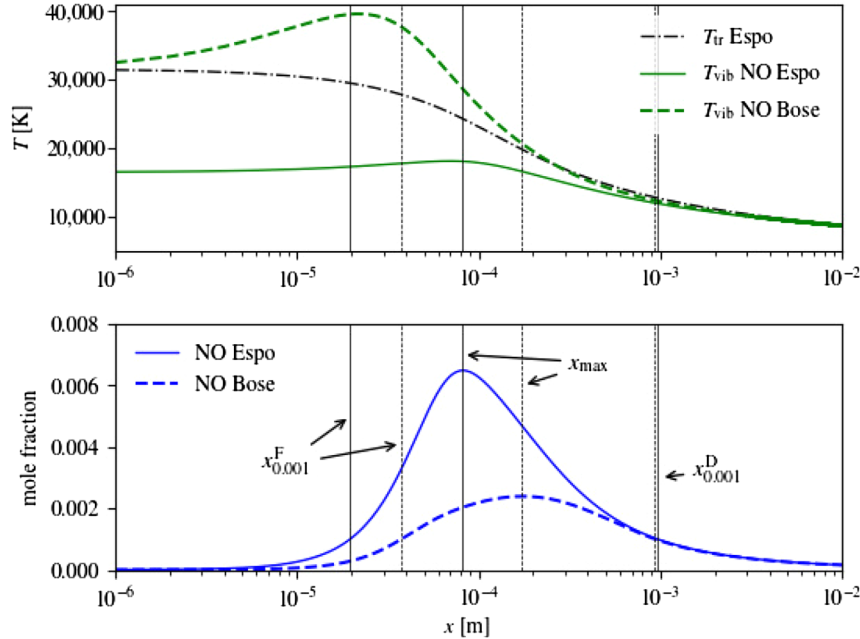


Fig. 10 Locations where vibrational distribution functions for NO are sampled ($u_1 = 8.06 \text{ km/s}$, $p_1 = 0.25 \text{ torr}$).

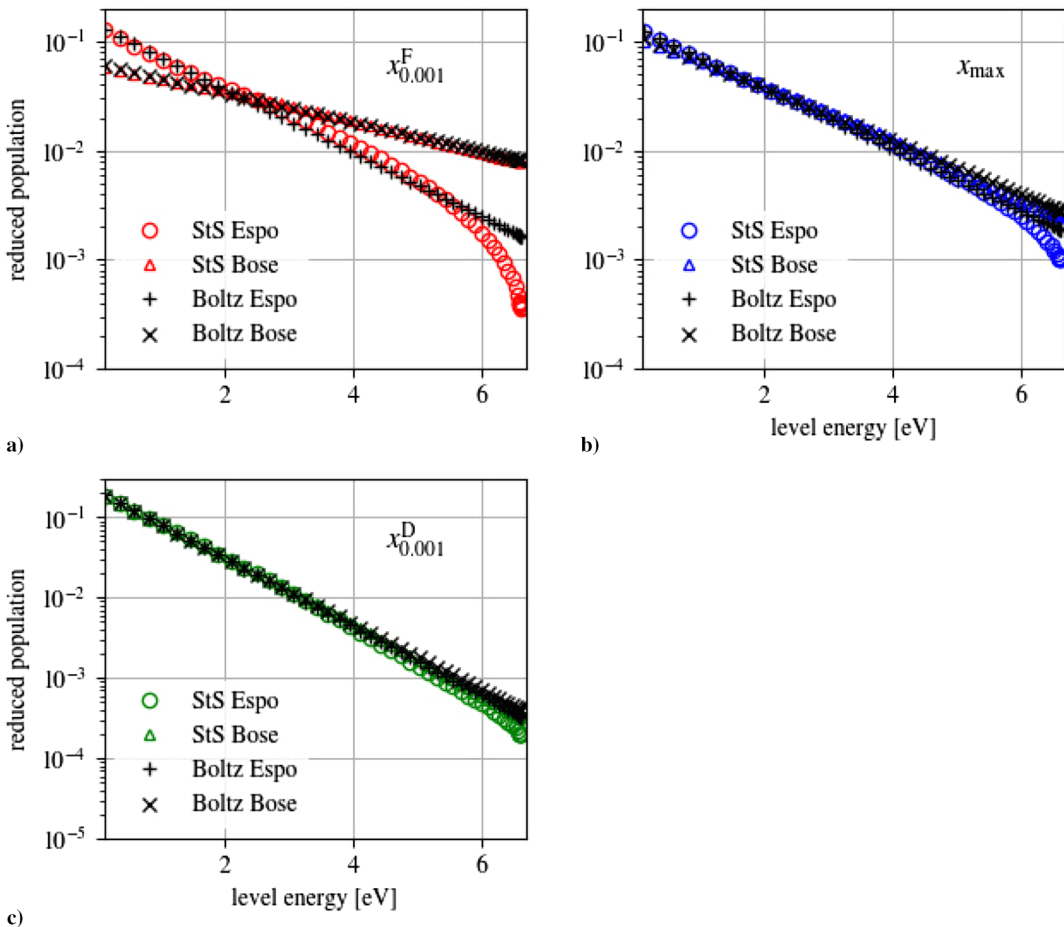


Fig. 11 Vibrational distribution functions of NO as obtained in the state-specific models. The Boltzmann distribution at the equivalent T_{vib} is also plotted for comparison: a) at $x_{0.001}^F$; b) at x_{max} ; c) at $x_{0.001}^D$.

IV. Flow Radiative Properties

A. Shock Layer Radiative Signature

To assess the performance of the models considered in this study, we have rebuilt the radiative signature of the postshock plasma and compared it with shock-tube measurements of spectral intensities in

the UV spectral range [21]. In this spectral range, plasma radiation is dominated by emission from the molecular electronic systems. The spectral emission coefficient of the plasma, at wave number σ , is then expressed as the sum of all bound–bound rovibronic transitions from upper level u to lower level l :

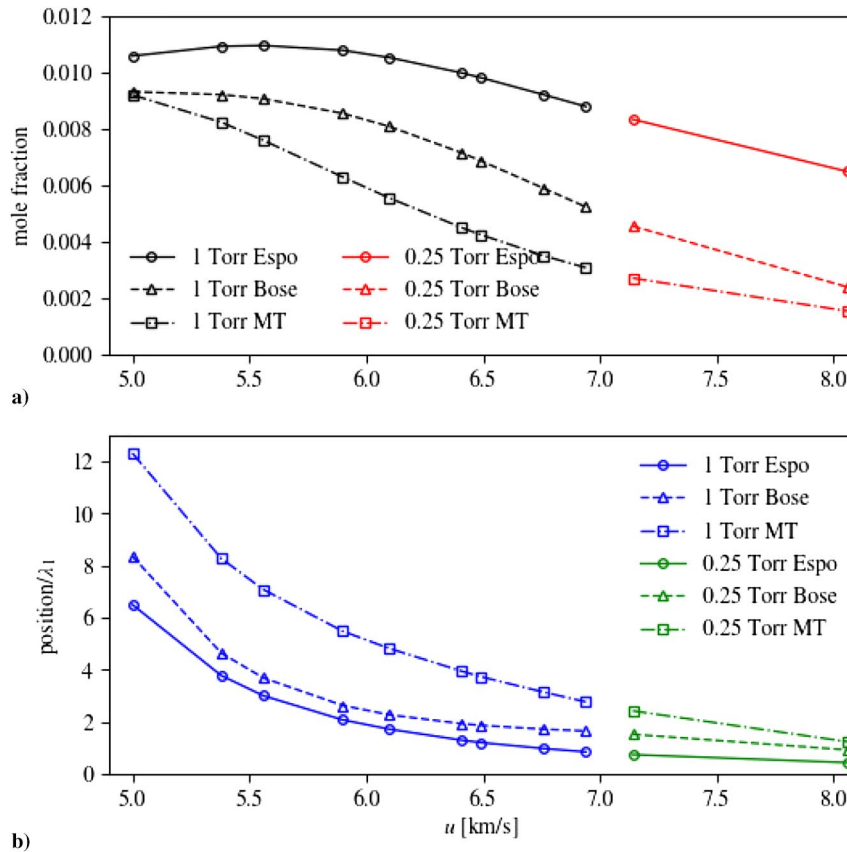


Fig. 12 Formation of NO as a function of shock speed: a) maximum mole fraction; b) position of the maximum (scaled by upstream mean free path).

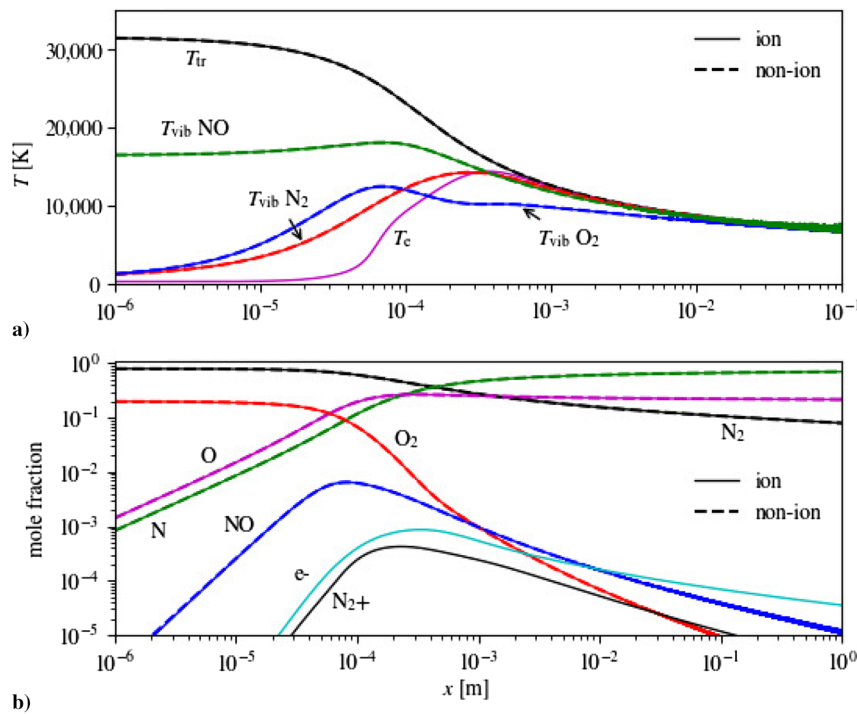


Fig. 13 Relaxation behind the shock ($u_1 = 8.06$ km/s, $p_1 = 0.25$ torr). Comparison of results obtained with the 5- and 11-species Espo model: a) temperature profiles; b) composition profiles.

$$\eta_\sigma = \sum_{ul} n_u \frac{A_{ul}}{4\pi} h c \sigma_{ul} f(\sigma - \sigma_{ul}) \quad (24)$$

where the line shape $f(\sigma - \sigma_{ul})$ only includes the effect of Doppler broadening because collisional broadening is negligible in the

present conditions. The emission coefficient has been calculated accounting for the electronic systems of N_2 , O_2 , NO, and N_2^+ , listed in Table 4, for which required spectroscopic data are taken from the high-resolution spectroscopic database HTGR [20], which includes an exhaustive set of vibrational bands up to the dissociation limit for each electronic state.

Table 4 Molecular bands contributing in the UV spectral range

Electronic system designation	Upper/lower states	Spectral range, nm	Calculated bands (0: v'_{\max} , 0: v''_{\max})
O ₂ , SR	B ³ Σ _u ⁻ – X ³ Σ _g ⁻	200–400	(0:19–0:21)
N ₂ , SP	C ³ Π _u – B ³ Π _g	270–400	(0:4–0:21)
N ₂ ⁺ , FN	B ² Σ _u ⁺ – X ² Σ _g ⁺	320–400	(0:8–0:21)
NO γ	A ² Σ ⁺ – X ² Π _r	200–270	(0:8–0:22)
NO β	B ² Π _r – X ² Π _r	200–270	(0:37–0:22)
NO β'	B ² Δ – X ² Π _r	200–270	(0:6–0:22)
NO δ	C ² Π _r – X ² Π _r	200–270	(0:9–0:22)
NO ϵ	D ² Σ ⁺ – X ² Π _r	200–270	(0:5–0:22)
NO γ'	E ² Σ ⁺ – X ² Π _r	200–270	(0:4–0:22)

For each diatomic molecular species, the population of the upper level n_u is calculated in the frame of the two-temperature model. Hence, for a rovibronic level identified by (n, v, J) , the electronic, vibrational, and rotational quantum numbers, respectively, its population density is calculated as

$$n_{uvJ} = n_{tot} \frac{g_{uvJ}}{Q(T_{rot}, T_{ve})} \times \exp\left(-\frac{\epsilon^{el}(n) + \epsilon^{vib}(n, v)}{k_B T_{ve}}\right) \times \exp\left(-\frac{\epsilon^{rot}(n, J) + \epsilon^{inter}(n, v, J)}{k_B T_{rot}}\right) \quad (25)$$

where n_{tot} is the total population of the species and $Q(T_{rot}, T_{ve})$ is the two-temperature partition function; ϵ^{vib} , ϵ^{rot} , $\epsilon^{inter}(n, v, J)$ refer to electronic-vibrational energy, rotational energy, and a rovibrational coupling term that is small in practice (for more details refer to [38]).

In the following, we consider the measurements of the plasma spectral intensity in the direction perpendicular to the flow (for details on the data acquisition system and the methodology, see [39]). The intensity, acquired by means of optical emission spectroscopy, corresponds to the local postshock plasma emission integrated along the flow diameter, where uniform properties are assumed along the transverse direction. The self-absorption in the UV spectral range has been assessed and was found to be negligible for the overall conditions considered here, therefore, the plasma will be considered in the following as optically thin. The transverse intensity $I_\sigma(x)$, at a position x downstream of the shock, is then obtained as

$$I_\sigma(x) = \eta_\sigma(x) \times D \quad (26)$$

where the shock diameter D is assumed to be equal to the shock-tube test section diameter 50 mm and $\eta_\sigma(x)$ is the emission coefficient at location x (along the flow axis).

Also, the acquisition time was set higher than the radiating flow lasting time, meaning that the collected radiation profile is not spatially resolved, but instead integrated along the flow axis. The intensity collected by the acquisition system is then calculated as

$$\bar{I}_\sigma = \frac{1}{\Delta x} \int_{\Delta x} I_\sigma(x) dx \quad (27)$$

where $\Delta x = v_{\text{shock}} \times t_{\text{rad}}$ is the length of the plasma axial extent, and t_{rad} refers to the effective duration of the plasma radiation when passing through the measurement test section of 6 and 17 μ s, respectively, for the 0.25 and 1 torr cases. Finally, for comparisons with measured spectra, the collected intensity is convoluted with the apparatus function approximated by a normalized Gaussian function with full-width half-maximum equal to 1.55 nm (2 nm).**

B. Results

The local emission profiles obtained in the UV range for background pressure $p_1 = 1.0$ torr are plotted in Figs. 14 and 15, respectively, for shock speed u_1 of 5.56 and 6.94 km/s. Plotted are

the total emission profiles predicted by MT and Esposito (ES) models, together with the specific contributions from N₂, O₂, and NO electronic systems. Because the emission profiles obtained with the Bose (BO) model differ only marginally from those obtained with the ES model, reflecting the differences in the predicted flow properties, they are not plotted (typically the difference is highest at the peak and achieves $\approx 8\%$ in the worst case). Also, the emission profile for N₂⁺ FN is not displayed because it remains always much smaller than the others. The effect of the model on the total emission profiles is rather small at $u_1 = 5.56$ km/s, differences being limited to about 10–12%. The O₂ Schumann–Runge (SR) emission dominates the peak emission, whereas the contribution of the other systems of NO and N₂ remains less than about 20%. Increasing the shock speed, differences become more significant. At $u_1 = 6.94$ km/s, the total emission at the peak location predicted by the MT model is three times greater than that obtained with the ES model, which is of the same order as that at $u_1 = 5.56$ km/s. For both models, the relative contribution of the N₂ second positive (SP) emission has increased and becomes comparable to that of the O₂ SR, whereas the emission of NO systems remains much smaller than the rest. The cumulated total emission profiles (i.e., the intensity obtained integrating the emission along the downstream direction) have also been reported to appreciate the relative contribution to the spatially integrated intensity of the emission from the peak region and from the postpeak emission region, designated by “plateau” hereafter. At the lower speed, the peak emission contributes roughly two-thirds of the cumulated emission. With shock speed increase, the flattening of the cumulated emission profile right after the peak is a consequence of the integrated plasma intensity being dominated by emission from the peak, where nonequilibrium conditions hold.

The noticeable effect of the model on the cumulated emission is consequently mirrored on the spectral distribution of the spatially integrated plasma intensity, which is the quantity directly comparable

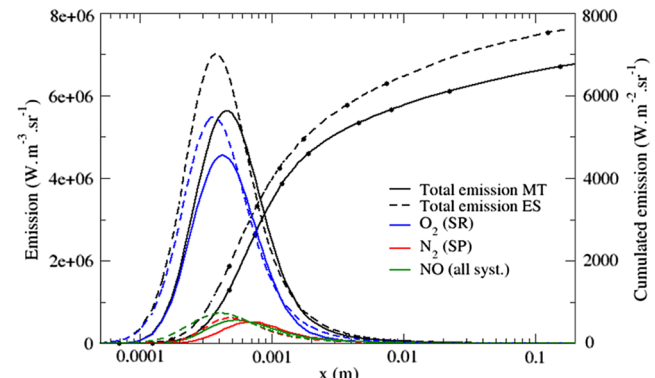


Fig. 14 Emission profiles calculated with ES and MT models and corresponding cumulated total emission profiles at $u_1 = 5.56$ km/s, $p_1 = 1.0$ torr.

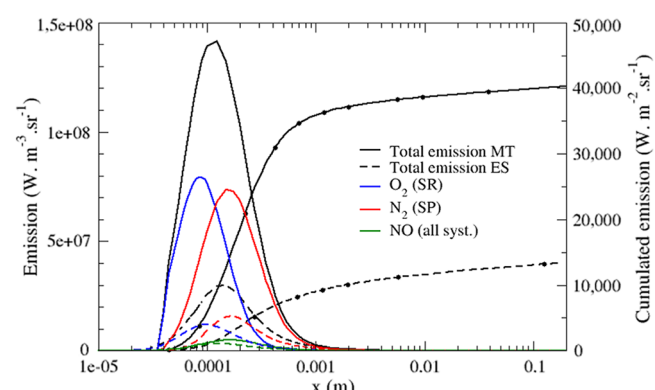


Fig. 15 Emission profiles calculated with ES and MT models and corresponding cumulated total emission profiles at $u_1 = 6.94$ km/s, $p_1 = 1.0$ torr.

**Pavel V. Kozlov, Institute of Mechanics, Lomonosov Moscow State University, Private Communication with P. Kozlov, 25 January 2016.

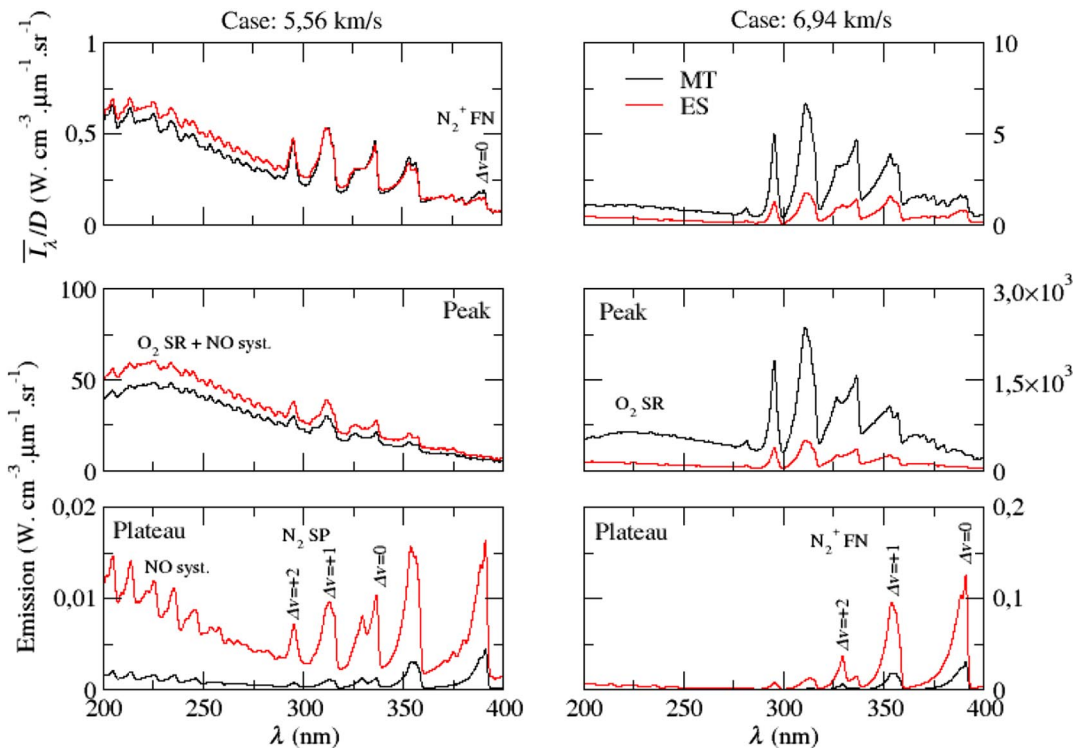


Fig. 16 UV spectral signature for (left) $u_1 = 5.56$ and (right) 6.94 km/s (from top to bottom: spatial average, peak region, plateau region).

to experimental measurements. Because of the integrated nature of the experimental spectra, their interpretations have to be conducted with special care. Indeed, the measured spectral intensity integrates the contributions from the peak, which is very intense over a short time, and from the so-called plateau, which is of much weaker intensity but lasts much longer. As a result, the integrated spectral intensity exhibits spectral features that are in the main associated with the most energetic region, which can be both (the peak or the plateau). To illustrate this point in our conditions, namely, the contribution from equilibrium and nonequilibrium regions to the postshock plasma UV radiative signature, the calculated spectral distributions of spatially integrated intensity and of local emission at the peak and at the plateau locations are gathered in Fig. 16.

In the case $u_1 = 5.56 \text{ km/s}$, the spectral intensity distribution follows the emission distribution at the peak, but it also includes a contribution from the plateau. For instance, the small contribution of the vibrational band sequence $\Delta v = 0$ of N_2^+ first negative (FN) peaking at about 380 nm, observed on the intensity, is absent from the peak emission and clearly prominent in the plateau. In the case $u_1 = 6.94$, as discussed previously, the plasma intensity originates mainly from the peak emission. The resulting spectral intensity is therefore very similar to the emission distribution in the peak and it is only weakly modified by the contribution of N_2^+ FN coming from the plateau.

Comparisons between spectral intensities obtained with the MT, ES, and BO models and measured radiative signatures at $p_1 = 1.0 \text{ torr}$ are gathered in Figs. 17 and 18, respectively, for the $u_1 = 5.56$ and 6.94 km/s cases. At the lower speed, all models provide a similar intensity distribution that, however, lies above the experimental one, except around 380 nm, where N_2^+ FN radiation is underpredicted (also true for higher shock speed).

In this spectral region, the measured intensity is dominated by the vibrational band sequence $\Delta v = 0$ of the CN violet system $B^2\Sigma^+ - X^2\Sigma^+$, whose contribution is corroborated by the presence of its vibrational band sequence $\Delta v = +1$, well visible at about 365 nm. Such contamination prevents elaboration of any definitive conclusion on the agreement obtained for N_2^+ FN.

At the higher speed, differences between the spectral intensities calculated by the state-specific models have faded. In the range below 270 nm, dominated by NO and O_2 radiation, if the MT model still

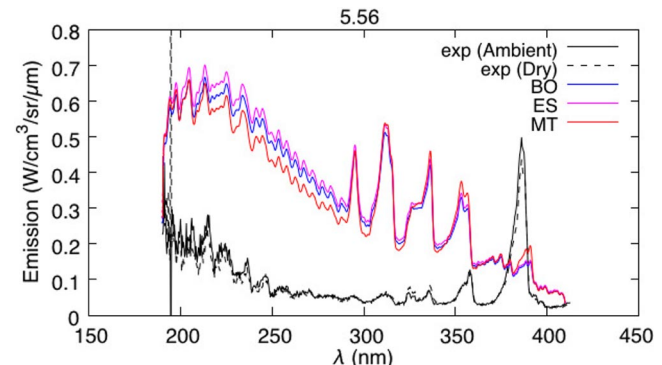


Fig. 17 Modeled and measured spectral intensities at $u_1 = 5.56 \text{ km/s}$.

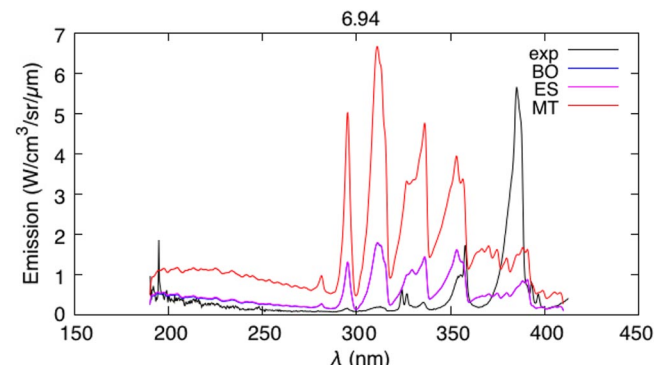
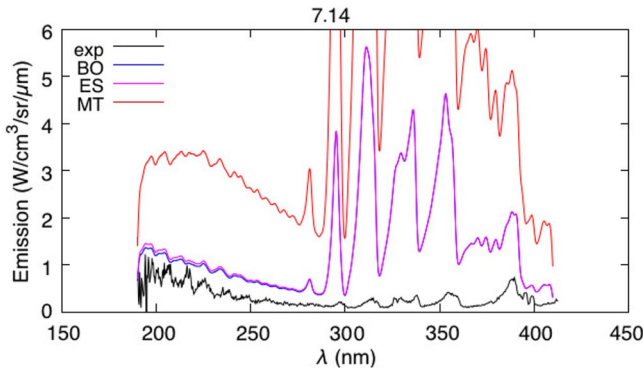
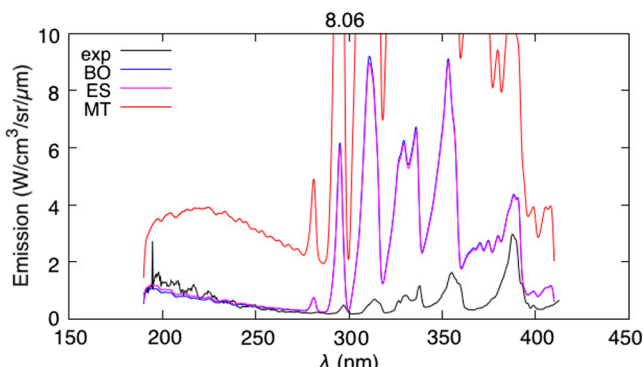


Fig. 18 Modeled and measured spectral intensities at $u_1 = 6.94 \text{ km/s}$.

overpredicts the intensity, the state-specific models yield instead a better agreement with measurements.

The spectral band observed at about 380 nm can be reasonably attributed to the band sequence $\Delta v = 0$ of N_2^+ FN, considering the agreement between predicted and experimental band shape. Though this band could most probably be mixed with CN violet system

Fig. 19 Modeled and measured spectral intensities at $u_1 = 7.14$ km/s.Fig. 20 Modeled and measured spectral intensities at $u_1 = 8.06$ km/s.

emission, we can, however, observe that the N_2^+ FN emission is overestimated. Radiation from N_2 is still overpredicted by all models.

Comparisons between simulated and measured spectra at $p_1 = 0.25$ torr are collected in Figs. 19 and 20, respectively, for $u_1 = 7.14$ and 8.06 km/s cases. As a rule, the intensity obtained with the MT model is systematically too high compared with the experimental data. The intensities predicted with the state-specific models exhibit instead a meaningful agreement with N_2^+ FN spectrum observed at 380 nm (band sequence $\Delta v = 0$), at variance from the high-pressure case.

The N_2 SP intensity is again poorly reproduced. In this case, whereas calculations predict a major contribution of the peak emission to the radiative signature, the experimental results seem to suggest an important contribution from the thermal equilibrium region. These differences may be explained by either underestimation of the N_2 dissociation in the nonequilibrium region or to an important role of quenching mechanisms for the radiating electronic states.

Below about 270 nm, acceptable agreement is found between experiment and predictions of the state-specific models. It is difficult, however, to disentangle contributions from the NO systems from the O_2 SR emission that overlap in this region.

Some insight can be obtained by looking at total intensities, obtained by integrating the spectral intensity distributions in the range between 200 and 270 nm, as a function of shock speed, for all shock speed conditions documented in [21]. The resulting values obtained with the MT and ES models are compared with the experimental ones in Fig. 21. Although uncertainty on measurements is not quoted in the cited work [21], it is roughly estimated assuming that the calibration procedure alone produces an uncertainty of 50% on the absolute intensity measurements (see footnote **).

MT values are systematically several times higher than experimental ones. Though they exhibit a monotonic increase with increasing shock speed, as in the experiment, the two trends are qualitatively different. For the higher pressure, the calculated intensity remains dominated by the O_2 SR radiation, which is

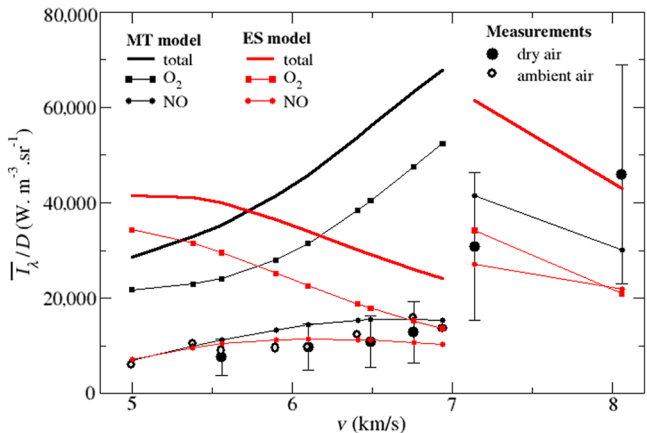


Fig. 21 Predicted and measured intensity integrated in the range 200–270 nm. Note that velocities below and above 7 km/s correspond, respectively, to background pressure of 1 and 0.25 torr.

responsible for more than 70% of the total intensity, and follows a polynomial-like rising trend.

ES values, instead, show a decreasing trend, so that agreement with experiment improves at larger shock speeds. This behavior reflects the predicted trend for the O_2 emission, whose importance, at variance from the MT model, decreases with increasing shock speed.

NO intensities obtained with MT and ES models exhibit a fair agreement. Both show a similar trend, albeit absolute values show differences increasing with the shock speed.

It is worth noting that NO-predicted intensities reproduce fairly accurately experimental measurements, suggesting that O_2 emission might be a source of systematic overestimation. Again, this can be due to underestimation of dissociation or to quenching mechanisms for the radiating electronic states.

It must be stressed that the simulated emission spectra are very sensitive to the free electron temperature that controls, in the present calculations, the population of the radiating electronic states. Indeed, by lowering the excitation temperature by 10% for the case $p = 1$ torr, $v = 5.0$ km/s, we obtained a significantly lower peak emission that reduced the difference between simulated and measured radiative signatures to within the experimental uncertainty (not shown here).

Measurements of emission intensities' temporal profiles would clarify the relative role of emission from the peak and the equilibrium regions, respectively, and would therefore be valuable for assessing the possible causes of the discrepancies.

From the preceding discussion, we conclude that available kinetic models are reliable enough to produce results comparable to experimental measurements. As a consequence, more stringent requirements are imposed on the accuracy of the model predictions (few percent on the excitation temperature, for example). It is therefore worth estimating the role of some modeling assumptions that, though widely accepted, can actually produce noticeable effects in the present context. First, rotational equilibrium has been assumed to occur instantaneously. In reality, rotational relaxation has been shown to proceed slowly at high temperatures [40], so that most of the vibrational relaxation zone will be in conditions of rotational nonequilibrium also. The gas temperature will be correspondingly larger. The two changes will compensate to some extent, but a study that takes into account the role of rotational energy on the rates is required to assess this point. Viscous effects, not considered here, can in principle smooth out the relaxation profiles. A simple estimation of the contribution of the Fourier heat flux to the energy conservation equation for the conditions studied reveals that the assumption of inviscid flow is indeed justified for all but the fastest shocks. For the latter, the viscous terms contribute up to 20% in the first few mean free paths. A consideration of these effects is therefore required to produce accurate predictions.

V. Conclusions

A detailed kinetic mechanism has been studied for describing the relaxation behind shock waves in air at shock speeds where radiation from diatomics is predominant. The mechanism is vibrationally specific for the electronic ground state of the neutral molecules involved. In particular, two sets of reaction rate coefficients for the Zeldovich reactions of NO formation, obtained from accurate QCT calculations, have been critically analyzed. Results show that the NO formation kinetics is sensitive to the details of the adopted rate coefficients. Both models predict larger NO formation and faster relaxation than the standard MT model; they also predict a large vibrational temperature for the nascent NO population. Because this does not come exclusively from nonequilibrium of the high vibrational levels and it also affects the population of low-lying levels, there is hope that it could be investigated by experimental measurements of the NO vibrational temperature. Results from the calculations have then been used to estimate the emitted radiation and compare it to shock-tube spectroscopic measurements of absolute intensities. No definitive conclusion could be drawn but the agreement is somewhat better for the state-specific models, even though significant discrepancies remain.

It is suggested that the inclusion of a kinetic model for the relevant electronic excited states (i.e., a collisional-radiative model) could improve the agreement with the experiment and that temporally resolved measurements of emission intensities could help in assessing the dynamics of different relaxation processes.

Acknowledgments

This project has received funding from the Universidad Carlos III de Madrid, the European Union's Seventh Framework Programme for research, technological development and demonstration under grant agreement N°600371, el Ministerio de Economía, Industria y Competitividad (COFUND2013-40258), el Ministerio de Educación, cultura y Deporte (CEI-15-17) and Banco Santander. The authors wish to thank P. V. Kozlov (Lomonosov Moscow State University) and S. T. Surzhikov (Institute for Problema in Mechanics, Russian Academy of Sciences) for useful discussions.

References

- [1] Lemal, A., Jacobs, C. M., Perrin, M.-Y., Laux, C. O., Tran, P., and Raynaud, E., "Prediction of Nonequilibrium Air Plasma Radiation Behind a Shock Wave," *Journal of Thermophysics and Heat Transfer*, Vol. 30, No. 1, 2016, pp. 197–210.
doi:10.2514/1.T4550
- [2] Bruno, D., Capitelli, M., Esposito, F., Longo, S., and Minelli, P., "Direct Simulation of Non-Equilibrium Kinetics Under Shock Conditions in Nitrogen," *Chemical Physics Letters*, Vol. 360, Nos. 1–2, 2002, pp. 31–37.
doi:10.1016/S0009-2614(02)00772-8
- [3] Kim, J. G., and Boyd, I. D., "State-Resolved Master Equation Analysis of Thermochemical Nonequilibrium of Nitrogen," *Chemical Physics*, Vol. 415, No. 1, 2013, pp. 237–246.
doi:10.1016/j.chemphys.2013.01.027
- [4] Panesi, M., Munafò, A., Magin, T. E., and Jaffe, R. L., "Nonequilibrium Shock-Heated Nitrogen Flows Using a Rovibrational State-to-State Method," *Physical Review E*, Vol. 90, No. 1, July 2014, Paper 013009.
doi:10.1103/PhysRevE.90.013009
- [5] Guy, A., Bourdon, A., and Perrin, M.-Y., "Consistent Multi-Internal-Temperature Models for Vibrational and Electronic Nonequilibrium in Hypersonic Nitrogen Plasma Flows," *Physics of Plasmas*, Vol. 22, No. 4, 2015, Paper 043507.
doi:10.1063/1.4917338
- [6] Munafò, A., Liu, Y., and Panesi, M., "Modeling of Dissociation and Energy Transfer in Shock-Heated Nitrogen Flows," *Physics of Fluids*, Vol. 27, No. 12, 2015, Paper 127101.
doi:10.1063/1.4935929
- [7] Lordet, F., Meolans, J. G., Chauvin, A., and Brun, R., "Nonequilibrium Vibration-Dissociation Phenomena Behind a Propagating Shock Wave: Vibrational Population Calculation," *Shock Waves*, Vol. 4, No. 6, 1995, pp. 299–312.
doi:10.1007/BF01413872
- [8] Andrienko, D. A., and Boyd, I. D., "Rovibrational Energy Transfer and Dissociation in O_2-O Collisions," *Journal of Chemical Physics*, Vol. 144, No. 10, 2016, Paper 104301.
doi:10.1063/1.4943114
- [9] Capitelli, M., Armenise, I., and Gorse, C., "State-to-State Approach in the Kinetics of Air Components Under Re-Entry Conditions," *Journal of Thermophysics and Heat Transfer*, Vol. 11, No. 4, Oct. 1997, pp. 570–578.
doi:10.2514/2.6281
- [10] Chauveau, S., Laux, C., Kelley, J., and Kruger, C., "Vibrationally-Specific Collisional-Radiative Model for Nonequilibrium Air Plasmas," *33rd Plasmadynamics and Lasers Conference*, AIAA Paper 2002-2229, May 2002.
- [11] Kunova, O., Nagnibeda, E., and Sharafutdinov, I., "State-to-State and Simplified Models for Shock Heated Reacting Air Flows," *AIP Conference Proceedings*, Vol. 1628, No. 1, 2014, pp. 1194–1201.
doi:10.1063/1.4902728
- [12] Lopez, B., and da Silva, M. L., "Non-Boltzmann Analysis of Hypersonic Air Re-Entry Flows," *11th AIAA/ASME Joint Thermophysics and Heat Transfer Conference*, AIAA Paper 2014-2547, June 2014.
- [13] Bose, D., and Candler, G. V., "Thermal Rate Constants of the $N_2 + O = NO + O$ Reaction Using Ab Initio 3A'' and 3A' Potential Energy Surfaces," *Journal of Chemical Physics*, Vol. 104, No. 8, 1996, pp. 2825–2833.
doi:10.1063/1.471106
- [14] Bose, D., and Candler, G. V., "Thermal Rate Constants of the $O_2 + N = NO + O$ Reaction Based on the A2' and A4' Potential-Energy Surfaces," *Journal of Chemical Physics*, Vol. 107, No. 16, 1997, pp. 6136–6145.
doi:10.1063/1.475132
- [15] Esposito, F., and Armenise, I., "Reactive, Inelastic and Dissociation Processes in Collisions of Atomic Oxygen with Molecular Nitrogen," *Journal of Physical Chemistry A*, Vol. 121, No. 33, 2017, pp. 6211–6219.
doi:10.1021/acs.jpca.7b04442
- [16] Armenise, I., and Esposito, F., "N₂, O₂, NO State-to-State Vibrational Kinetics in Hypersonic Boundary Layers: The Problem of Rescaling Rate Coefficients to Uniform Vibrational Ladders," *Chemical Physics*, Vol. 446, No. 1, 2015, pp. 30–46.
doi:10.1016/j.chemphys.2014.11.004
- [17] Capitelli, M., Celiberto, R., Colonna, G., Esposito, F., Gorse, C., Hassouni, K., Laricchiuta, A., and Longo, S., *Reactivity and Relaxation of Vibrationally/Rotationally Excited Molecules with Open Shell Atoms*, Vol. 85, Springer Series on Atomic, Optical, and Plasma Physics, Springer-Verlag, New York, 2016, pp. 31–56, Chap. 2.
- [18] Andrienko, D. A., and Boyd, I. D., "Thermal Relaxation of Molecular Oxygen in Collisions with Nitrogen Atoms," *Journal of Chemical Physics*, Vol. 145, No. 1, 2016, Paper 014309.
doi:10.1063/1.4955199
- [19] Luo, H., Kulakhmetov, M., and Alexeenko, A., "Ab Initio State-Specific N₂ + O Dissociation and Exchange Modeling for Molecular Simulations," *Journal of Chemical Physics*, Vol. 146, No. 7, 2017, Paper 074303.
doi:10.1063/1.4975770
- [20] Perrin, M. Y., Riviere, P., and Soufiani, A., "Radiation Database for Earth and Mars Entry," *Proceedings of the AVT-162 RTO AVT/VKI Lecture Series*, von Karman Inst., Rhode St. Gen'ese, Belgium, Sept. 2008; also RTO-ENAVT-162-08, 2009.
- [21] Dikalyuk, A., Kozlov, P., Romanenko, Y., Shatalov, O., and Surzhikov, S., "Nonequilibrium Spectral Radiation Behind the Shock Waves in Martian and Earth Atmospheres," *44th Thermophysics Conference*, AIAA Paper 2013-2505, June 2013.
- [22] Radhakrishnan, K., and Hindmarsh, A., "Description and Use of LSODE, the Livermore Solver for Ordinary Differential Equations," NASA RP-1327, Washington, D.C., 1993.
- [23] Zeldovich, Y. B., Sadovnikov, P. Y., and Frank-Kamenetskii, D. A., "Oxidation of Nitrogen in Combustion," Academy of Sciences, USSR, Moscow-Leningrad, 1947.
- [24] Da Silva, M. L., Lopez, B., Guerra, V., and Loureiro, J., "A Multiquantum State-to-State Model for the Fundamental States of Air and Application to the Modeling of High-Speed Shocked Flows," *Proceedings of the Fifth International Workshop on Radiation of High Temperature Gases in Atmospheric Entry*, edited by L. Ouwehand, ESA Communications, European Space Research and Technology Centre, ESA SP-714, Noordwijk, The Netherlands, Dec. 2012.
- [25] Adamovich, I. V., Macheret, S. O., Rich, J. W., Treanor, C. E., and Fridman, A. A., "Vibrational Relaxation, Nonequilibrium Chemical Reactions, and Kinetics of NO Formation Behind Strong Shock Waves," *Molecular Physics and Hypersonic Flows SE-5*, edited by M. Capitelli, Vol. 482, NATO ASI Series, Springer Netherlands, Dordrecht, The Netherlands, 1996, pp. 85–104.

- [26] Esposito, F., Armenise, I., and Capitelli, M., “N–N₂ State to State Vibrational-Relaxation and Dissociation Rates Based on Quasiclassical Calculations,” *Chemical Physics*, Vol. 331, No. 1, 2006, pp. 1–8.
doi:10.1016/j.chemphys.2006.09.035
- [27] Esposito, F., Armenise, I., Capitta, G., and Capitelli, M., “O–O₂ State-to-State Vibrational Relaxation and Dissociation Rates Based on Quasiclassical Calculations,” *Chemical Physics*, Vol. 351, Nos. 1–3, 2008, pp. 91–98.
doi:10.1016/j.chemphys.2008.04.004
- [28] Sayos, R., Oliva, C., and Gonzalez, M., “New Analytical (²A'/⁴A') Surfaces and Theoretical Rate Constants for the N(⁴S) + O₂ Reaction,” *Journal of Chemical Physics*, Vol. 117, No. 2, 2002, pp. 670–679.
doi:10.1063/1.1483853
- [29] Gamallo, P., Gonzalez, M., and Sayos, R., “Ab Initio Derived Analytical Fits of the Two Lowest Triplet Potential Energy Surfaces and Theoretical Rate Constants for the N(⁴S) + NO(X²Π) System,” *Journal of Chemical Physics*, Vol. 119, No. 5, 2003, pp. 2545–2556.
doi:10.1063/1.1586251
- [30] Akpinar, S., Armenise, I., Defazio, P., Esposito, F., Gamallo, P., Petrongolo, C., and Sayos, R., “Quantum Mechanical and Quasiclassical Born–Oppenheimer Dynamics of the Reaction N₂ + O → N + NO on the N₂O a3A'' and b3A' Surfaces,” *Chemical Physics*, Vol. 398, No. 4, 2012, pp. 81–89.
doi:10.1016/j.chemphys.2011.05.005
- [31] Millikan, R. C., and White, D. R., “Systematics of Vibrational Relaxation,” *Journal of Chemical Physics*, Vol. 39, No. 12, 1963, pp. 3209–3213.
doi:10.1063/1.1734182
- [32] Park, C., *Nonequilibrium Hypersonic Aerothermodynamics*, 1st ed., Wiley-Interscience, New York, 1990.
- [33] Laporta, V., Celiberto, R., and Wadehra, J. M., “Theoretical Vibrational-Excitation Cross Sections and Rate Coefficients for Electron-Impact Resonant Collisions Involving Rovibrationally Excited N₂ and NO and Molecules,” *Plasma Sources Science and Technology*, Vol. 21, No. 5, 2012, Paper 055018.
doi:10.1088/0963-0252/21/5/055018
- [34] Laporta, V., Celiberto, R., and Tennyson, J., “Resonant Vibrational-Excitation Cross Sections and Rate Constants for Low-Energy Electron Scattering by Molecular Oxygen,” *Plasma Sources Science and Technology*, Vol. 22, No. 2, 2013, Paper 025001.
doi:10.1088/0963-0252/22/2/025001
- [35] Laporta, V., Little, D. A., Celiberto, R., and Tennyson, J., “Electron-Impact Resonant Vibrational Excitation and Dissociation Processes Involving vibrationally excited N₂ Molecules,” *Plasma Sources Science and Technology*, Vol. 23, No. 6, 2014, Paper 065002.
doi:10.1088/0963-0252/23/6/065002
- [36] Laporta, V., Celiberto, R., and Tennyson, J., “Dissociative Electron Attachment and Electron-Impact Resonant Dissociation of vibrationally excited O₂ Molecules,” *Physical Review A: General Physics*, Vol. 91, Jan. 2015, Paper 012701.
doi:10.1103/PhysRevA.91.012701
- [37] Kim, M., Gulhan, A., and Boyd, I. D., “Modeling of Electron Energy Phenomena in Hypersonic Flows,” *Journal of Thermophysics and Heat Transfer*, Vol. 26, No. 2, Jan. 2012, pp. 244–257.
doi:10.2514/1.T3716
- [38] Babou, Y., Riviere, P., Perrin, M.-Y., and Soufiani, A., “High-Temperature and Nonequilibrium Partition Function and Thermodynamic Data of Diatomic Molecules,” *International Journal of Thermophysics*, Vol. 30, No. 2, 2009, pp. 416–438.
doi:10.1007/s10765-007-0288-6
- [39] Kozlov, P. V., Romanenko, Y. V., and Shatalov, O. P., “Radiation Intensity Measurement in Simulated Martian Atmospheres on the Double Diaphragm Shock Tube,” *Proceedings of the Fourth International Workshop on Radiation of High Temperature Gases in Atmospheric Entry*, edited by H. Lacoste-Francis, ESA Communications, European Space Research and Technology Centre, ESA SP-689, Noordwijk, The Netherlands, 2011.
- [40] Da Silva, M. L., Loureiro, J., and Guerra, V., “Rotational Nonequilibrium in State-Resolved Models for Shock-Heated Flows,” *Chemical Physics*, Vol. 398, April 2012, pp. 96–103.
doi:10.1016/j.chemphys.2011.08.014